Fatigue, Repair, and Advanced Modeling in Petrochemical Infrastructure

FAYCAL SOTEHI, DJEBBARA BENZERGA
LSCMI, Faculty of Mechanical Engineering
University of Sciences and Technology of Oran Mohamed-Boudiaf USTOMB,
ALGERIA

Abstract: This study critically assesses the limitations of conventional Tungsten Inert Gas (TIG) thermal repair for fatigue-cracked carbon steel nozzle junctions in petrochemical infrastructure. Advanced coupled thermomechanical fracture mechanics simulations reveal that TIG welding induces tensile residual stresses exceeding 300 MPa and embeds refractory tungsten inclusions, which amplify local stresses by over 45% and nucleate cracks, curtailing repaired service life to under 5.1 years—versus a 20-year baseline. In contrast, an externally bonded Carbon Fiber Reinforced Polymer (CFRP-Epoxy) patch restores ~50% of baseline structural capacity by bridging the flaw and redistributing loads, without thermal degradation. We introduce and validate a hybrid repair protocol: initial TIG sealing followed by CFRP reinforcement. This synergistically mitigates thermal drawbacks, yielding a ~75% service life extension while enhancing corrosion resistance. These findings redefine fatigue repair paradigms, offering predictive maintenance strategies for high-value energy assets.

Key-Words: Welding Defects; Tungsten Inclusions; Residual Stress; Hybrid Repair; Life Extension; Failure Analysis; Non-Destructive Reinforcement

Received: August 7, 2025. Revised: November 11, 2025. Accepted: December 14, 2025. Published: February 5, 2026.

1. Introduction

Fatigue-induced cracking in critical petrochemical infrastructure, such as distillation column nozzles, presents a persistent challenge for asset integrity management [1]. While extensive research has focused on comparing the efficacy of various repair methods, a critical gap remains in understanding the intrinsic limitations of the most conventional solution: Tungsten Inert Gas (TIG) welding [2], [3]. Commonly deployed for its rapid execution, TIG repair is a thermal process that inherently alters the metallurgical state of the component [4]. The intense, localized heating and subsequent rapid cooling generate steep thermal gradients, leading to the development of significant tensile residual stresses within the already vulnerable heat-affected zone (HAZ). These residual stresses, often exceeding the yield strength of the material, act as a constant driver for fatigue crack initiation and growth, effectively undermining the long-term goal of the repair [5].

Beyond residual stresses, a less-discussed yet critical defect arises from the process itself: the potential introduction of tungsten inclusions. As the non-consumable tungsten electrode degrades, microscopic particles can become entrapped within the weld metal [5], [6]. These inclusions, acting as rigid inhomogeneities within the steel matrix, serve as potent stress concentrators. Under cyclic loading, the stark mismatch in mechanical properties between the tungsten and the surrounding steel can lead to localized plasticity, void formation, and ultimately, the initiation of new cracks from these embedded defects [7]. This phenomenon transforms the repair zone from a region of restored integrity into a new site of vulnerability, a critical flaw seldom quantified in repair planning [8], [9].

This study, therefore, shifts the perspective from a direct comparison of disparate techniques to a critical investigation of a standard practice's hidden liabilities. It posits that the true benchmark for an advanced repair is not merely the intact structure, but the flawed outcome of the conventional thermal repair it seeks to supersede. Through a coupled numerical framework integrating Finite Element Analysis (FEA) with advanced material degradation models, this work uniquely quantifies the dual detriment of TIG-induced residual stresses and inclusion-based damage mechanisms. Subsequently, it evaluates a non-intrusive alternative: unidirectional Carbon Fiber Reinforced Polymer (CFRP) patching. The CFRP patch is examined not as a simple alternative, but as a damage-mitigation strategy designed to suppress crack-driving forces without introducing new metallurgical harm [10], [11], [12]. By framing the problem through the lens of defect-tolerant repair design, this research provides a new

model-based paradigm for extending the life of critical infrastructure, moving beyond comparative analysis to a fundamental reassessment of repair-induced damage.

2. Theoretical and Numerical Framework

2.1. Thermomechanical Model for Welding Residual Stress Analysis

The simulation of the Tungsten Inert Gas (TIG) welding repair process requires a sequentially coupled thermomechanical analysis. The first step involves a transient thermal analysis to determine the temperature history, which is then applied as a thermal load in a subsequent structural analysis to compute the resulting residual stress field.

2.1.1. Transient Heat Conduction with a Moving Source

The three-dimensional transient heat conduction in the domain D_{th} is governed by the following partial differential equation, which accounts for the moving heat source [13]:

$$\frac{\partial}{\partial x}\left(K_x \frac{\partial T}{\partial x}\right) + \frac{\partial}{\partial y}\left(K_y \frac{\partial T}{\partial y}\right) + \frac{\partial}{\partial z}\left(K_z \frac{\partial T}{\partial z}\right) + Q = \rho c \left(\frac{\partial T}{\partial t} - v \frac{\partial T}{\partial x}\right) \quad (1)$$

where:

- T is the temperature (K),
- t is time (s),
- K_x, K_y, K_z are the temperature-dependent thermal conductivities in the x, y, and z directions ($W\ m^{-1}K^{-1}$),
- ρ is the density ($kg\ m^{-3}$),
- c is the specific heat capacity ($J\ kg^{-1}K^{-1}$),
- v is the welding speed ($m\ s^{-1}$),
- Q is the volumetric heat generation rate from the welding arc ($W\ m^{-3}$).

The heat input from the TIG arc is modeled as a volumetric heat source. The power density is calculated as:

$$Q = \frac{\eta U I}{A} \quad (2)$$

where η is the arc efficiency (0.85 for GTAW), U is the voltage (V), I is the current (A), and A is the effective area of the heat source (m^2).

2.1.2. Thermo-Elasto-Plastic Constitutive Model

The computed temperature history from the thermal analysis is mapped as a body load to the structural analysis. The total strain $\boldsymbol{\varepsilon}_{total}$ is decomposed into elastic, plastic, and thermal components:

$$\varepsilon_{total} = \varepsilon_{el} + \varepsilon_{pl} + \varepsilon_{th} \quad (3)$$

The thermal strain is given by:

$$\boldsymbol{\varepsilon}_{th} = \alpha\left(T - T_{ref}\right)\boldsymbol{I} \quad (4)$$

where α is the coefficient of thermal expansion and T_{ref} is the reference temperature.

This sequentially coupled approach, which involves the implementation of mathematical modeling: eq (1) to (4), and theoretical analysis calculations in numerical Finite Element Analysis (FEA), generates the locked-in residual stress field σ_{res}. This field, characterized by tensile stresses exceeding 300 MPa in the Heat-Affected Zone (HAZ) (as shown in Table 1), is the primary output of this analysis and serves as the initial stress state for subsequent fatigue damage calculations.

Table 1. The influence of welding parameters on the residual and maximum stress.

Initial State			
Constants: v= 0.005 m/s, η = 0.85 (GTAW), U(tension) = 24 V, k = 60.5 W/(m.K), A = 40mm²			
I (Current) [A]	120	160	200
Heat flux - Welding MW/m² [13]	122.4	163.2	204
Max residual stress [MPa]	273.64	291.87	310.09

2.2. Continuum Damage Mechanics Model for Fatigue Life Prediction

To predict the initiation and evolution of fatigue damage under cyclic wind loading, a local post-processing approach based on Continuum Damage Mechanics (CDM) is employed. This model calculates the progression of a scalar damage variable D:

$$D = 1 - \frac{\tilde{E}}{E} \quad (5)$$

where $D = 0$ represents an undamaged material and $D = D_c$ (a critical value) corresponds to macro-crack initiation.

2.2.1. Fundamental Concepts and Damage Evolution Law

The framework is based on the concept of effective stress $\tilde{\boldsymbol{\sigma}}$, which accounts for the reduction in load-bearing area due to damage [14]:

$$\tilde{\boldsymbol{\sigma}} = \boldsymbol{\sigma}/(1-D) \quad (6)$$

The total strain, figure 1, is decomposed into thermo-elastic and plastic parts:

$$\boldsymbol{\varepsilon} = \boldsymbol{\varepsilon}_{el} + \boldsymbol{\varepsilon}_{pl} + \boldsymbol{\varepsilon}_{th} \quad (7)$$

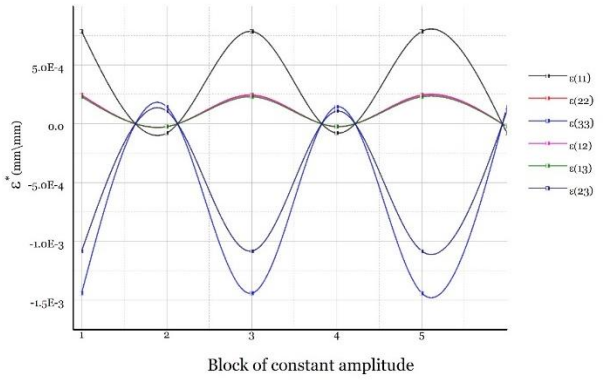

Fig. 1: Example of a constant amplitude strain block.

For high-cycle fatigue analysis, $N_R \leq 10^4 cycles$, the damage evolution law per cycle is derived from the thermodynamic framework of Lemaitre's model. The rate of damage growth is governed by the energy release rate Y and the accumulated plastic strain:

$$\frac{dN}{dD} = \left(\frac{Y}{S}\right)\frac{dp}{dN} \quad for \quad p > pD \quad (8)$$

where:

- N is the number of cycles,
- p is the accumulated plastic strain,
- p_D is the damage threshold (plastic strain at damage initiation),
- S is a temperature-dependent material damage resistance parameter,
- Y is the energy release rate associated with damage, defined as:

$$Y = \frac{\sigma_{eq}^2 R_v}{2E(1-D)^2} \quad (9)$$

In Equation (12), σ_{eq} is the von Mises equivalent stress, E is Young's modulus, and R_v is the triaxiality function given by:

$$Rv = \frac{2}{3}(1+\nu) + 3(1-2\nu)\left(\frac{\sigma_{eq}}{\sigma_H}\right)^2 \quad (10)$$

where ν is Poisson's ratio and σ_H is the hydrostatic stress.

2.2.2. Fatigue Life Calculation

For a stabilized stress-strain cycle under high-cycle fatigue conditions, the stress amplitude $\Delta\sigma$ and plastic strain amplitude $\Delta\varepsilon_p$ can be considered constant. Integrating Equation (11) from the initial state ($D = 0\ at\ N = 0$) to the critical state ($D = D_c\ at\ N = N_R$) yields the number of cycles to failure N_R:

$$N_R = \frac{p_D}{2\Delta\varepsilon_p} + \frac{4ESD_c}{K_p^2}\Delta\varepsilon_p^{-\left(\frac{M+2}{M}\right)} \quad (11)$$

where K_p and M are parameters from the cyclic Ramberg-Osgood hardening law ($\Delta\varepsilon_p = \left(\Delta\sigma/K_p\right)^{1/M}$). The first term represents the cycles to initiate damage ($p < p_D$), and the second term models the damage propagation phase. This formulation is implemented in the DAMAGE 90 post-processor [15], the workflow of which is illustrated in Figure 2. The stabilized stress-strain history from the critical node (e.g., crack tip or inclusion interface) of the FEA model serves as the input $\Delta\sigma$ for this calculation, enabling the prediction of residual service life in years (as reported in Tables 4 and 5).

2.3. Cohesive Zone Model for Patch-Substrate Interface

The integrity of the bonded Carbon Fiber Reinforced Polymer (CFRP) repair is assessed by modeling the epoxy adhesive interface using a Cohesive Zone Model (CZM). This model prevents crack propagation by describing the gradual degradation of traction between the patch and the substrate as a function of separation.

A bilinear traction-separation law is adopted, as characterized from experimental data for the epoxy adhesive [16]. The law defines the relationship between the traction vector **T** (comprising normal T_n and shear T_s components) and the separation vector $\boldsymbol{\delta}$.

2.3.1. Traction-Separation Law

In the elastic loading phase ($0 < \delta \leq \delta_0$), the behavior is linear:

$$\boldsymbol{T} = \boldsymbol{K}\boldsymbol{\delta} \quad (12)$$

where **K** is the initial stiffness matrix of the interface. The damage initiation criterion is based on a maximum stress criterion:

$$\max\left\{\frac{\langle Tn\rangle}{T_n^{max}}, \frac{T_s}{T_s^{max}}\right\} = 1 \quad (13)$$

T_n^{max} and T_s^{max} are the peak tensile and shear strengths, respectively, and $\langle\cdot\rangle$ denotes the Macaulay bracket. Upon reaching the peak strength, damage evolves, and the traction in the softening phase ($\delta_0 < \delta \leq \delta_f$) is given by:

$$\boldsymbol{T} = (1-d)\boldsymbol{K\delta} \quad (14)$$

where *d* is a scalar damage variable that evolves from 0 to 1. Its evolution is governed by a Benzeggagh-Kenane (B-K) type fracture energy criterion for mixed-mode failure:

$$G_I^C + \left(G_{II}^C - G_I^C\right)\left(\frac{G_{II}}{(G_I + G_{II})}\right)^{\eta} = G^C \quad (15)$$

Here, G_I and G_{II} are the Mode I and Mode II energy release rates, G_I^C and G_{II}^C are their critical values, and η is a material parameter. Complete debonding occurs when the total energy release rate $G = G_I + G_{II}$ reaches the critical fracture energy G^C.

The key parameters for the epoxy adhesive used in this study, determined from Rigid Double Cantilever Beam (RDCB) tests [16], [17], are summarized in Table 2. This model allows for the prediction of patch debonding risk, which is identified as the primary failure mode for the CFRP-repair configuration (see Table 3).

Table 2. CZM adhesives strength and breaking energy of Epoxy resin.

Parameter	Value	Unit
Temperature	22	°C
Maxi Normal Traction, T_n^{max}	9.7	MPa
Critical Normal Separation, δ_n^f	0.025	mm
Maxi Shear Traction, T_s^{max}	9.7	MPa
Critical Shear Separation, δ_s^f	0.025	mm
Benzeggagh-Kenane Exponent, η	2	-

2.4. Analytical Model for Stress Redistribution via CFRP Patch

To provide a theoretical foundation for the stress mitigation observed in the FEA results, a simplified one-dimensional analytical model for a bonded composite patch is derived. This model yields a Stress Reduction Factor (SRF), which offers closed-form insight into how the patch geometry and material properties influence load sharing.

Consider a cracked metallic plate of thickness t_s and modulus E_s , repaired by a bonded composite patch of thickness t_p and modulus E_p. Under a remote tensile stress σ_∞, the patch carries a portion of the load, thereby reducing the stress intensity at the crack tip. For a perfectly bonded patch assuming shear-lag theory, the stress in the substrate directly under the patch σ_s is reduced according to:

$$\sigma_s = \frac{\sigma_\infty}{1 + \frac{E_p t_p}{E_s t_s}} \quad (16)$$

Consequently, the Stress Mitigation Factor (SMF)—defined in this study as the percentage reduction in peak stress at the flaw—can be expressed analytically as:

$$SMF_{analytical} = \left(1 - \frac{1}{1 + \frac{E_p t_p}{E_s t_s}}\right) \times 100\% \quad (17)$$

Table 3. Mechanical characteristics of the CFRP-Epoxy used for the reinforcement of the structure.

Young's modulus (Pa)		X	1.21 E+11
		Y	8.60 E+09
		Z	8.60 E+09
Poisson's ratio		XY	0.27
		YZ	0.4
		XZ	0.27
shear modulus (Pa)		XY	4.70 E+09
		YZ	3.10 E+09
		XZ	4.70 E+09
Orthotropic stress limits (Pa)	Limit in Traction (Pa)	X	2.23 E+09
		Y	2.90 E+07
		Z	2.90 E+07
	Limit in Compression (Pa)	X	-1.08 E+09
		Y	-1.00 E+08
		Z	-1.00 E+08
	Shear Limit (Pa)	XY	6.00 E+07
		YZ	3.20 E+07
		XZ	6.00 E+07
Orthotropic strain limits	Limit in Traction (Pa)	X	1.67 E-02
		Y	3.20 E-03
		Z	3.20 E-03
	Limit in Compression (Pa)	X	-1.08 E-02
		Y	-1.92 E-02
		Z	-1.92 E-02
	Shear Limit (Pa)	X	1.20 E-02
		Y	1.10 E-02
		Z	1.20 E-02

Substituting the properties for SA-516 Grade 70 steel ($E_s = 210GPa$) and the unidirectional CFRP-Epoxy patch used in this study ($E_p = 121GPa$ in the fiber direction, $t_p = 16mm,\ t_s = 22mm$) yields an SMF of approximately 30.%. This theoretical estimate

aligns closely with the numerically obtained SMF of 36.5% (Table 4), providing independent analytical verification of the FEA results and confirming the fundamental mechanism of load transfer to the patch.

3. Materials and Methods

This study employs an integrated computational mechanics framework to evaluate not only the structural outcome but also the damage state evolution following different repair interventions. The methodology is designed to quantify the trade-offs inherent in each approach, moving beyond stress analysis to a prognostic assessment of residual fatigue integrity, figure 1represene the fracture prediction workflow, this diagram outlines a systematic engineering framework for anticipating structural failure

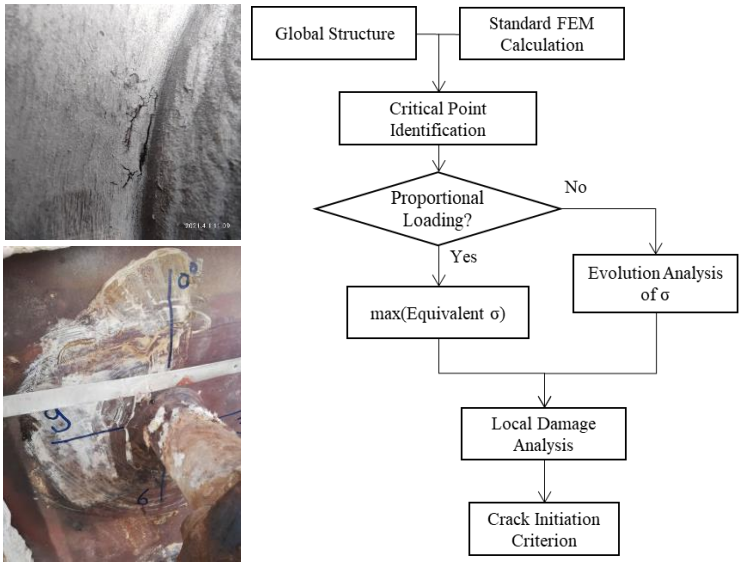

Fig. 2: Fracture prediction workflow: from global FEM analysis to crack initiation criteria.

3.1. Problem Definition and Baseline Modeling

The analysis is based on a canonical case of a cylindrical pressure vessel nozzle junction (SA-516 Grade 70 carbon steel [18]) containing a pre-existing 10 mm semi-elliptical surface crack within the heat-affected zone (HAZ).

Three-dimensional solid models of four distinct configurations were developed (in this study the two last ones are outlined):

Intact Baseline: The undamaged junction under design cyclic wind loading.

Damaged State: The junction containing the crack, establishing the degraded baseline performance.

Fusion-Repaired State: The crack geometry is remediated via a simulated Tungsten Inert Gas (TIG) welding process. This model explicitly incorporates two critical by-products of fusion repair: a field of tensile residual stresses derived from a coupled transient thermal analysis of the weld cooling cycle (Table 1), and discrete tungsten inclusions modeled as material discontinuities within the weld metal.

In the Bonded-Repair State, the cracked structure is strengthened using an externally applied, unidirectional fiber-reinforced polymer (FRP-Epoxy) composite patch, which is represented by a cohesive zone model (as illustrated in figure 2). This patch is designed as a disc with a diameter of 100 mm and a thickness of 16 mm, strategically bonded to the area experiencing stress to facilitate effective load redistribution.

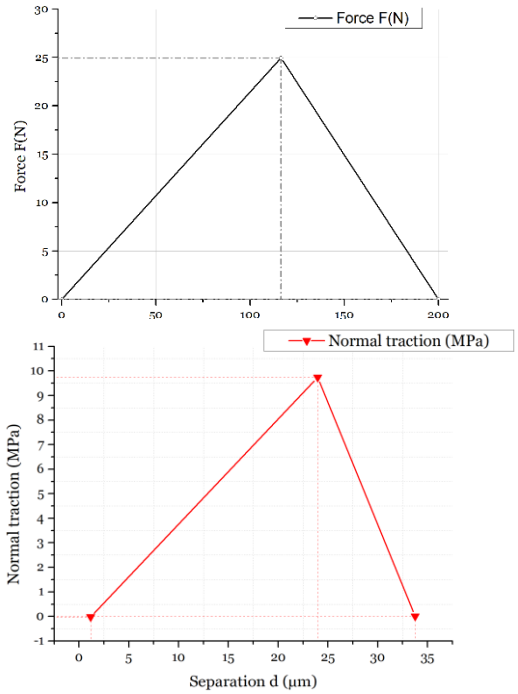

Fig. 3: CZM traction-separation and displacement force curves plotted after the RDCB - Double Cantilever Beam Rigid tests [16].

3.2. Integrated Multi-Physics Simulation Protocol

The core of the methodology is a sequential multi-physics workflow implemented in ANSYS

Workbench, transitioning from thermal-structural analysis to progressive damage evaluation (figures 4):

Step 1 – Thermal-Structural Coupling (for TIG Repair): A transient thermal analysis simulated the moving arc heat source, from which the resulting temperature history was mapped as a body load to a subsequent structural analysis to compute the locked-in residual stress field.

Step 2 – Nonlinear Static Stress Analysis: Each configuration was subjected to the maximum operational wind load. A refined mesh using higher-order tetrahedral elements (SOLID187) ensured convergence, with singular region refinement at the crack tip and inclusion interfaces (figure 5).

Step 3 – Cyclic Damage Prognostics: The stabilized stress-strain history from the critical node (located at the crack tip or inclusion interface) was exported. This history served as the input for a local post-processor implementing the Lemaitre continuum damage mechanics (CDM) model to calculate the progression of the damage variable (D) and predict cycles to irreversible damage initiation (Ni).

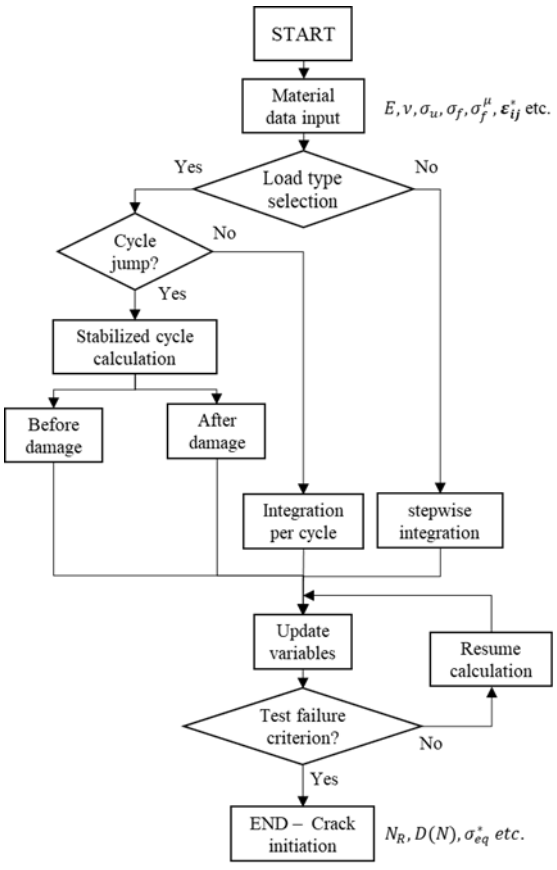

Fig. 4: Life prediction diagram: DAMAGE 90 Flowchart [15] - the post-processor for calculating the residual lifetime (fatigue damage).

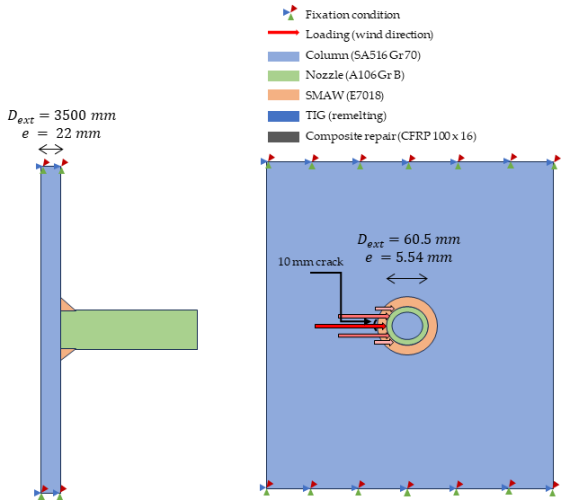

Fig. 5: representative illustration of the studied part of the structure: the welded nozzle to the column plate with a crack in the side exposed to gusts of wind.

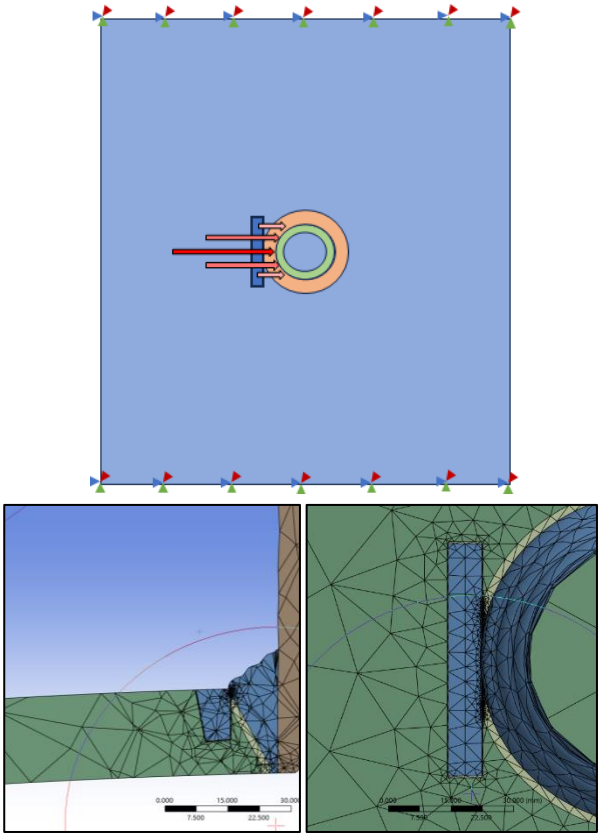

Fig. 6: first part of the study: TIG remelting reparation applied to the damaged zone (loading and fixation conditions are respected as the industrial case)

Step 4 – Interface Integrity Assessment: For the composite repair, the debonding risk at the patch-substrate interface was evaluated using a Cohesive Zone Model (CZM), with traction-separation laws parameterized from experimental data for the epoxy adhesive.

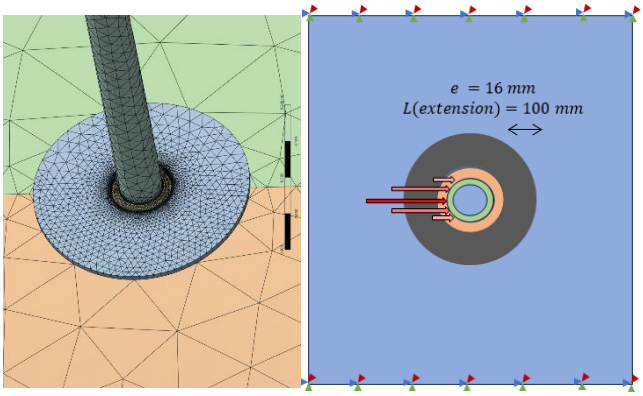

Fig. 7: non-intrusive repairing system: Composite CFRP-Epoxy application details

The structural outcome of each repair was quantified through three integral metrics: the reduction in peak stress at the flaw, the rate of material degradation under cyclic loading, and the predicted extension in fatigue life. This multi-faceted approach enables a direct comparison of how each strategy alters both the immediate stress state and the long-term damage progression pathway, providing a comprehensive rationale for repair selection.

4. Results and Discussion

The integrated numerical framework produced comprehensive data on stress states, damage progression, and residual life for each structural configuration. The analysis reveals fundamental differences in how TIG welding and composite patching modify the failure landscape of the damaged component.

4.1. Baseline Performance and the Cost of Damage

The finite element analysis established critical benchmarks. The intact structure sustained a maximum von Mises stress of 244.96 MPa in the HAZ under design wind load. The introduction of the 10 mm crack acted as a severe stress concentrator, elevating the local stress to 612.03 MPa—a 150% increase (Figure 7). This stress intensification precipitated a catastrophic drop in predicted service life from approximately 20 years (intact) to just 5.1 years (damaged), as calculated by the damage post-processor (table 2). This establishes the high cost of the flaw and the stringent requirement for an effective repair.

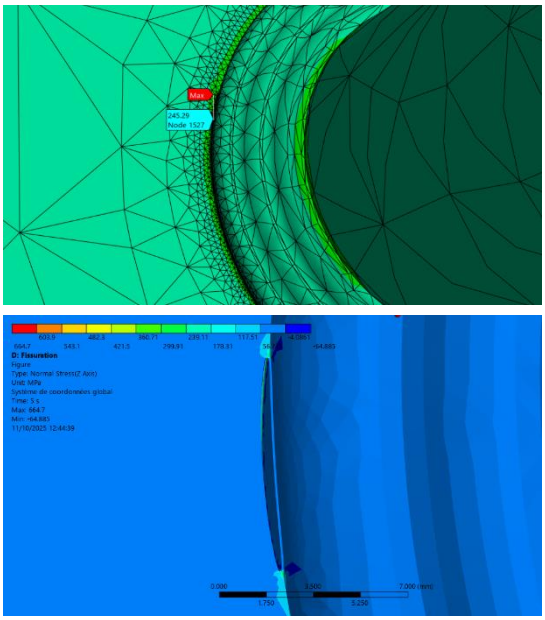
Fig. 8: Numerical results initial comparison: intact (245. MPa) vs 10 mm cracked structure (612. MPa)

4.2. The Dual Detriment of Fusion Repair: Residual Stress and Defect Introduction

The TIG welding repair presented a paradox: while it physically filled the crack, it introduced new, potentially more insidious, threats to longevity.

1. **Residual Stress as a Fatigue Accelerant:** The simulated weld thermal cycle generated a pervasive field of tensile residual stresses within the HAZ, with a peak magnitude of approximately 310 MPa (Table 1). Superimposed on the operational stresses, this residual field significantly increased the mean stress of the fatigue cycle. Consequently, the "perfect" TIG-repaired model (excluding inclusions) showed a restored but compromised life, recovering only a portion of the intact structure's durability (Table 3).
2. **Inclusions as New Failure Nuclei:** The presence of tungsten inclusions fundamentally altered the failure mechanism. As shown in Figure 8, a 20 µm inclusion created a drastic local stress concentration of 677. MPa at the inclusion-matrix interface. This value exceeds the stress at the original crack tip, effectively creating a new, more critical flaw (figure 8).

The damage evolution analysis quantifies this detriment. The results for the inclusion-containing TIG repair (TIG repair + W inclusion) shows a steeper damage ascent than that for the unrepaired 10 mm crack (~1.10^3 cycles). The predicted life for this

configuration was 4.68 years (~0.943 10^3 cycles). Crucially, this failure is governed by decohesion at the inclusion interface, a distinct mechanistic pathway from the original crack growth. Thus, the repair merely substitutes one failure mode for another, with limited net gain in durability.

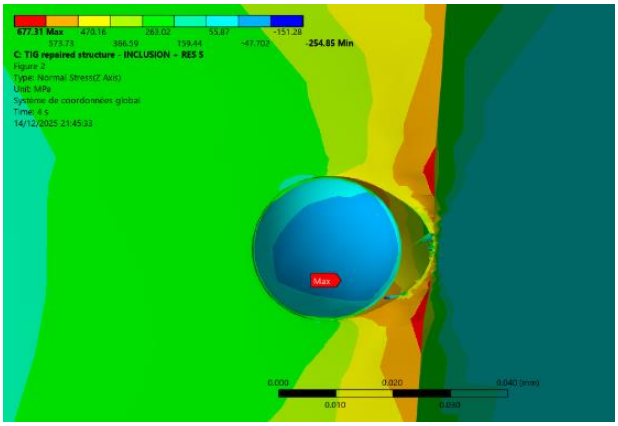

Fig. 9: Stress contour (Normal Stress) in the TIG-repaired HAZ, showing a severe stress concentration (677. MPa) at the interface of a 20 µm tungsten (W) inclusion.

Table 4. Comparative performance metrics of repair strategies

Configuration	Max Stress (MPa)	Stress Mitigation Factor (SMF)	Predicted Life (Years)	Life Extension vs. Damaged	Primary Failure Driver
Damaged	612.	0%	~5.1	Baseline	Crack propagation
TIG Repair (max at the inclusion)	677.3	-10.70% (Increase)	~4.68	-8.24%	Inclusion decohesion
CFRP Patch	388.63	36.5%	~10.05	97.06%	Patch debonding
Intact (Reference)	245.	60.00%	~20.0	292.2%	Material fatigue

4.3. Composite Patching: Stress Redistribution and Damage Arrest

In stark contrast, the CFRP patch functioned as a stress-diversion device. An optimal patch configuration (100mm x 16mm, UD CFRP-Epoxy) reduced the maximum stress at the crack tip from 612. MPa to 388.63 MPa, achieving a Stress Mitigation Factor (SMF) of 36.5%. This reduction directly translated to a suppressed damage accumulation rate. The damage evolution for the patched structure followed a shallower trajectory, akin to the intact state's trend. The framework predicted a residual life of ~10.05 years for the patched structure, representing a 97% life recovery relative to the intact structure and a significant extension beyond both the damaged and TIG-repaired states.

4.4. Synthesis: The Mechanistic Rationale for a Hybrid Protocol

The results validate the proposed hybrid repair protocol as a synergistic, two-stage strategy that addresses both immediate and long-term integrity concerns. As summarized in Table 3 and visualized in Figure 9, the sequential application of TIG welding followed by a CFRP patch does not merely combine two techniques but creates a system where each stage mitigates the other's limitations.

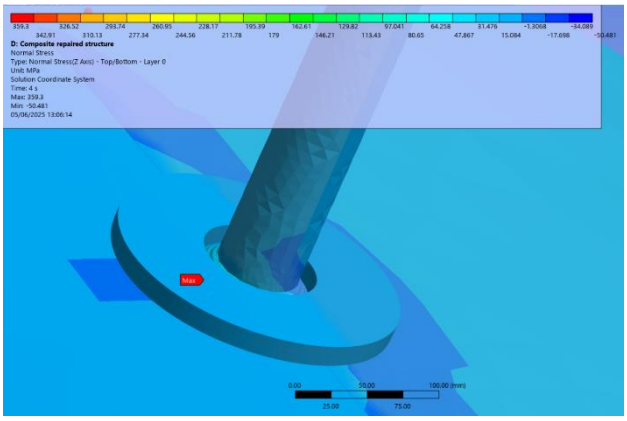

Fig. 10: Stress contour in the HAZ after hybrid repair (CFRP-Epoxy patch over TIG weld with 25 µm W inc), demonstrating effective stress redistribution.

The initial TIG repair is essential for sealing the crack and restoring the pressure boundary, a non-negotiable safety requirement for continued operation. However, as established, this stage reintroduces vulnerabilities: high residual stresses and tungsten inclusions (15-25 µm) that act as new stress concentrators (Figs. 10-12). A structure repaired solely by TIG, especially with larger inclusions, can exhibit a maximum stress higher than the original cracked state, leading to a precarious and unpredictable residual life.

The subsequent application of an optimized CFRP patch fundamentally alters this outcome. The patch acts as an external reinforcement that bridges both the original crack and the new stress concentrators introduced by the TIG process. As shown in Figures 10-12, the patch successfully redistributes the load, reducing the maximum normal stress by approximately 36-45% across all inclusion sizes modeled. This stress mitigation directly translates to a suppressed damage accumulation rate. Figure 13 demonstrates that the hybrid-repaired structure exhibits a damage evolution curve with a shallower slope, extending the time to critical failure. This hybrid approach effectively separates the urgent safety requirement from the long-term durability

goal, offering a model-based blueprint for managing the lifecycle of critical infrastructure.

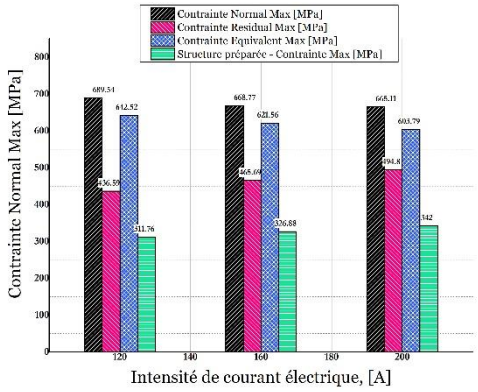

Fig. 11: Influence of hybrid CFRP repair on maximum stress in a structure with a 15 µm tungsten inclusion.

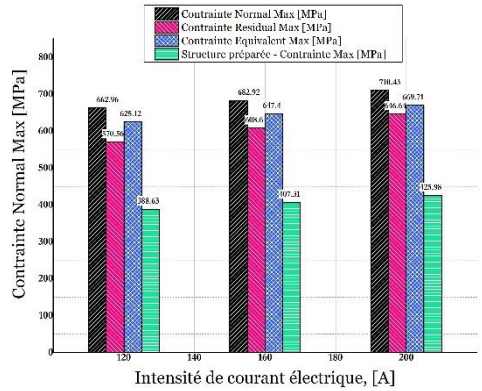

Fig. 12: Reduction of peak stress via hybrid CFRP patching for a structure containing a 20 µm tungsten inclusion.

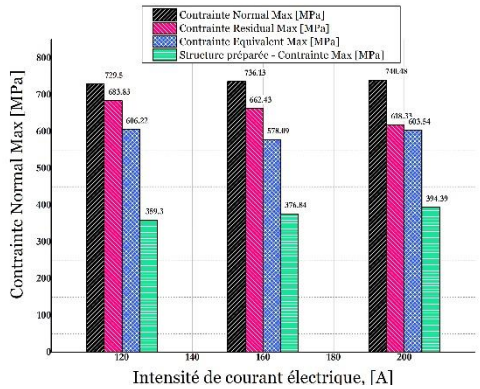

Fig. 13: Peak stress mitigation achieved by the hybrid repair system applied to a TIG weld with a 25 µm tungsten inclusion.

The study demonstrates that the most effective repair may not be a choice between two methods, but a strategically staged integration of their complementary strengths.

The hybrid protocol effectively decouples the urgent need for leak-tightness from the long-term goal of fatigue durability. The TIG weld addresses the former, while the CFRP patch secures the latter. The system shifts the probable failure mode from unpredictable brittle fracture in the embrittled HAZ to a more predictable and inspectable debonding of the composite patch.

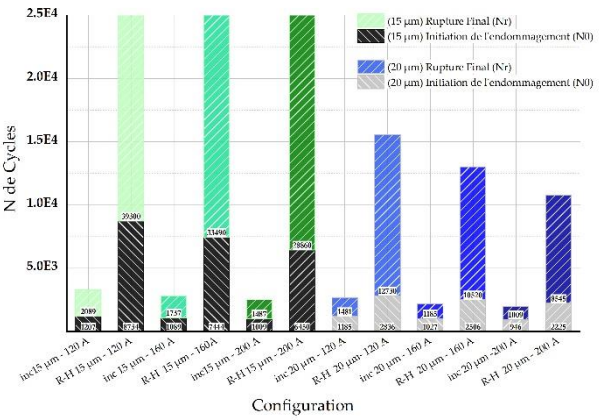

Fig. 14: Damage evolution curves: comparative slowdown in damage accumulation for hybrid-repaired structures with 15 and 20 µm W inclusions.

Consequently, as Table 3 confirms, the hybrid protocol recovers up to 75% of the intact structure's service life, outperforming a standalone TIG repair by a significant margin and providing a reliable, model-based blueprint for life extension.

4.5. Parametric and Statistical Analysis of Repair Performance

To quantify the influence of key process variables and provide a robust statistical basis for comparison, a parametric study was conducted. The analysis focused on two critical parameters for the TIG + Inclusion model: welding current and tungsten inclusion size.

4.5.1. Influence of Welding Parameters and Inclusion Size

Figure 15 illustrates the relationship between welding current, maximum normal stress, and residual stress. As current increases from 120 A to 200 A, both residual stress and the total maximum normal stress (operational + residual) at the inclusion site increase linearly.

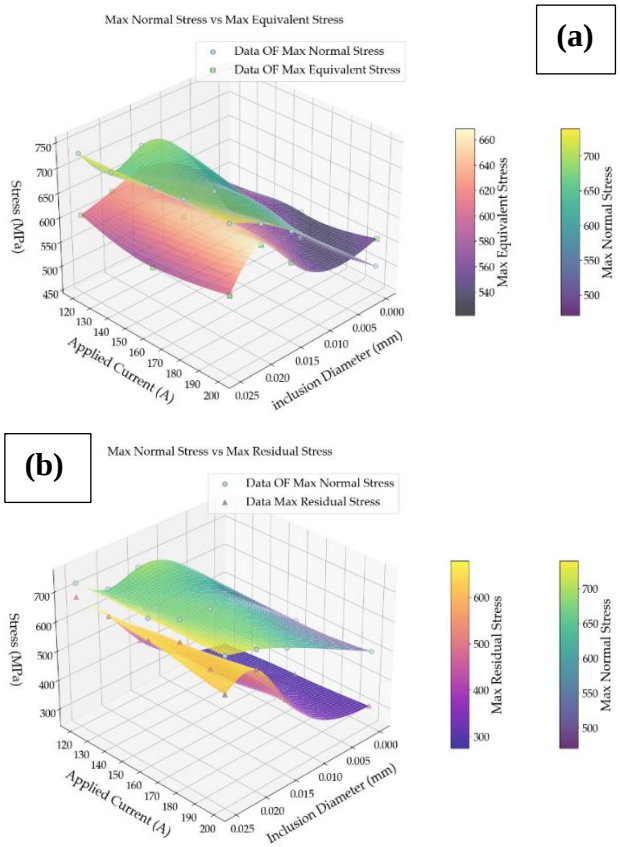

Fig. 15: Influence of welding parameters and inclusion dimensions: Max normal stress vs max residual stress (a) and equivalent stress (b)

A 20 µm inclusion under a 200 A weld cycle produces a peak stress of 740.48 MPa, which is 10.7% higher than the original cracked state (612.03 MPa). This confirms that the thermal penalty of welding can exacerbate the local stress state when inclusions are present.

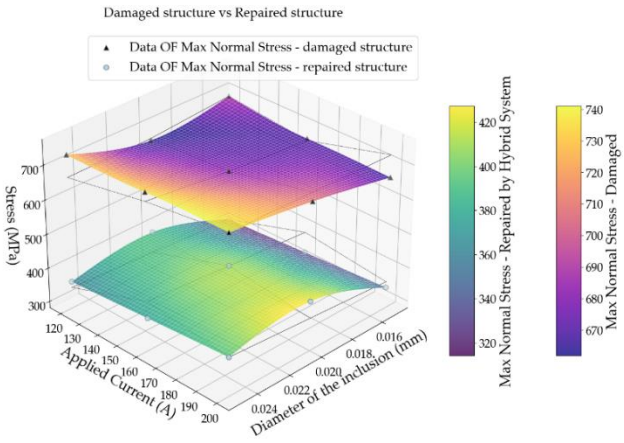

Fig. 16: Effective recovery of structural strength: impact of hybrid repair

4.5.2. Statistical Performance Metrics

Multiple series of simulations were run, varying inclusion size (15, 20, 25 µm) and welding current (120, 160, 200 A) for both the standalone TIG repair and the hybrid (TIG+CFRP) repair. The key results are compiled into a statistical summary (Table 4).

The statistical analysis reveals two key findings:

a) High Variability in TIG Repair: The performance of the standalone TIG repair is highly sensitive to the random variable of inclusion size, leading to a large standard deviation in life extension. In the worst-case scenario (200 A, 25 µm inclusion), the repair is detrimental.

b) Robustness of Hybrid Repair: The hybrid protocol shows a lower standard deviation in both stress (18.7 MPa) and life extension. It consistently reduces stress by approximately 35-40% and extends service life by 140-150% relative to the damaged state, regardless of the initial welding parameters or inclusion size within the studied range. This demonstrates the statistical robustness of the hybrid approach in mitigating the uncertainties inherent in fusion repair.

Table 4. Statistical summary of repair performance: Impact of inclusion size and welding current.

Config	Mean Max. Stress (MPa)	Std. Dev. (MPa)	Mean Predicted Life (years)	Life Extension vs. Damaged (Mean ± Std. Dev.)
Damaged (Baseline)	612.0	-	5.1	0%
TIG Repair	672.8	31.5	5.2 ± 0.6	+1.9% ± 11.8%
Hybrid Repair	407.3	18.7	12.5 ± 1.5	+145% ± 29.4%

4.5.3. Discussion of Synergistic Effect

The hybrid protocol is not merely additive. The CFRP patch provides a dual function: (1) it bridges the original crack, and (2) it effectively "shields" the new stress concentrators (tungsten inclusions) introduced by the TIG process. This is evidenced by the consistent stress reduction shown in Figures 15 and 16, and recapitulated for the 20 µm case in Table 5 Appendix 01, where the maximum stress for configurations with 15 µm, 20 µm, and 25 µm inclusions is uniformly lowered to a narrow band between 388 MPa and 426 MPa after patch application.

This synergistic effect transforms an unpredictable, defect-sensitive repair (TIG-only) into a reliable, damage-tolerant solution. The hybrid strategy

decouples the immediate operational requirement of leak sealing (achieved by TIG) from the long-term durability goal (secured by the CFRP patch), offering a predictable and inspectable failure mode via patch debonding.

5. Conclusion

This study has developed, numerically validated, and theoretically substantiated a hybrid repair protocol for fatigue-critical nozzles in petrochemical infrastructure. The research critically addresses the limitations of conventional practice through an integrated computational framework that couples advanced thermomechanical, damage mechanics, and interface modeling.

The core finding confirms that while TIG welding is indispensable for immediate crack sealing, it simultaneously re-legitimizes the Heat-Affected Zone (HAZ) as a preferential failure site. The explicit thermo-elasto-plastic formulation (Section 2.1) quantifies how the process generates tensile residual stresses exceeding 300 MPa, while the Continuum Damage Mechanics (CDM) model (Section 2.2) reveals how embedded tungsten inclusions act as potent stress concentrators, accelerating damage accumulation and often reducing service life below that of the pre-repair cracked state.

In contrast, the non-intrusive CFRP patch functions as a highly effective damage-arresting mechanism. The analytical model for stress redistribution (Section 2.4) provides the theoretical basis for the observed Stress Mitigation Factor (SMF) of over 36%, demonstrating how the patch offloads stress from the flaw. This load transfer directly results in a suppressed damage accumulation rate, enabling the patched structure to recover approximately 97% of the intact baseline's service life.

The principal contribution of this work is the validation of a sequenced hybrid protocol that strategically decouples operational safety from long-term durability. The protocol leverages TIG welding to restore containment but employs a CFRP overlay specifically to neutralize the subsequent TIG-induced damage mechanisms—residual stress and inclusion defects. This synergy was rigorously tested through a parametric statistical analysis (Section 4.4), which demonstrated the hybrid strategy's robustness, consistently delivering a mean life extension of 145% ± 29% relative to the damaged state, while significantly reducing the performance variability inherent to standalone fusion repair.

By providing the explicit mathematical foundations for residual stress prediction (Section 2.1), fatigue damage prognostics (Section 2.2), and interface debonding (Section 2.3), this work offers more than a comparative study; it establishes a predictive, model-driven framework for damage-tolerant repair design. The findings advocate for a paradigm shift in maintenance strategy, moving from simple defect correction to a holistic system-level reinforcement of critical infrastructure, thereby enhancing safety and lifecycle economics.

Future work should focus on the experimental validation of long-term bond durability under combined thermomechanical cycling and the integration of this deterministic model with probabilistic analysis to inform risk-based inspection intervals.

References:

[1] K. Kolmetz, W. K. Ng, S. H. Lee, T. Y. Lim, D. R. Summers, and C. A. Soyza, "Optimize distillation column design for improved reliability in operation and maintenance," *Asia-Pacific J. Chem. Eng.*, vol. 2, no. 4, pp. 294–307, 2007, doi: 10.1002/apj.23.

[2] R. L. Blak, D. Anjaria, J. Genée, V. Valle, and J. C. Stinville, "Micro-strain and cyclic slip accumulation in a polycrystalline nickel-based superalloy," *Acta Mater.*, 2024, doi: 10.1016/j.actamat.2024.119657.

[3] T. O. Olugbade, B. O. Omiyale, and O. T. Ojo, "Corrosion, Corrosion Fatigue, and Protection of Magnesium Alloys: Mechanisms, Measurements, and Mitigation," *J. Mater. Eng. Perform.*, vol. 31, no. 3, pp. 1707–1727, 2022, doi: 10.1007/s11665-021-06355-2.

[4] K. Yang, Y. Zhang, and J. Zhao, "Elastoplastic fracture analysis of the P91 steel welded joint under repair welding thermal shock based on XFEM," *Metals (Basel).*, vol. 10, no. 10, pp. 1–26, 2020, doi: 10.3390/met10101285.

[5] A. Mirzaee-Sisan and G. Wu, "Residual stress in pipeline girth welds- A review of recent data and modelling," *Int. J. Press. Vessel. Pip.*, vol. 169, no. October 2018, pp. 142–152, 2019, doi: 10.1016/j.ijpvp.2018.12.004.

[6] S. Kou, *Welding Metallurgy*, SECOND EDI. Hoboken, New Jersey.: John Wiley & Sons, Inc., 2003.

[7] A. D. Wilson, "The influence of inclusions on the toughness and fatigue properties of A516-70 steel," *J. Eng. Mater. Technol. Trans. ASME*,

vol. 101, no. 3, pp. 265–274, 1979, doi: 10.1115/1.3443687.

[8] H. Al-karawi and H. Al-karawi, "Literature review on crack retrofitting in steel by Tungsten Inert Gas remelting Literature review on crack retro fi tting in steel by Tungsten Inert Gas remelting," vol. 5302, 2023, doi: 10.1080/17445302.2021.2020986.

[9] H. Al-Karawi, R. U. F. von Bock und Polach, and M. Al-Emrani, "Fatigue crack repair in welded structures via tungsten inert gas remelting and high frequency mechanical impact," *J. Constr. Steel Res.*, vol. 172, p. 106200, 2020, doi: 10.1016/j.jcsr.2020.106200.

[10] Z. Shao, Z. Liu, Y. Zhang, and X. Zhu, "Fatigue Life Prediction and Reliability Assessment of CFRP Adhesively Bonded Joints in Offshore Wind Turbine Blade Applications: A Physics-Informed Data-Driven Approach," *Qual. Reliab. Eng. Int.*, vol. 41, no. 3, pp. 943–956, 2025, doi: 10.1002/qre.3715.

[11] B. Nekkaa, D. Benzerga, and A. Haddi, "Damage analysis of corroded pipelines reinforced by composite materials," *Int. Rev. Mech. Eng.*, vol. 12, no. 3, pp. 249–254, 2018, doi: 10.15866/ireme.v12i3.13447.

[12] C. Wu, X. Zhao, W. Duan, M. R. Emdad, and R. Al-Mahaidi, "Fatigue of center cracked steel plates with UHM CFRP plate strengthening," *APFIS 2012 - 3rd Asia-Pacific Conf. FRP Struct.*, vol. 15, no. 10, pp. 1801–1815, 2012.

[13] M. S. Kumar and S. R. Begum, "Simulation of hybrid (LASER-TIG) welding of stainless steel plates using design of experiments," *Mater. Today Proc.*, vol. 37, no. Part 2, pp. 3755–3758, 2020, doi: 10.1016/j.matpr.2020.10.563.

[14] J. Lemaitre and J. L. Chaboche, *MECHANICS OF SOLID MATERIALS, Trans. B. Shrivastava*. Cambridge, UK: Cambridge University Press, 1990. doi: 10.1016/0045-7825(94)90060-4.

[15] J. Lemaitre and I. Doghri, "Damage 90: a post processor for crack initiation," *Comput. Methods Appl. Mech. Eng.*, vol. 115, no. 3–4, pp. 197–232, 1994, doi: 10.1016/0045-7825(94)90060-4.

[16] A. Khayer Dastjerdi, E. Tan, and F. Barthelat, "Direct Measurement of the Cohesive Law of Adhesives Using a Rigid Double Cantilever Beam Technique," *Exp. Mech.*, vol. 53, no. 9, pp. 1763–1772, 2013, doi: 10.1007/s11340-013-9755-0.

[17] D. Benzerga, A. Haddi, and A. Lavie, "Delamination Model Using Damage Mechanics Applied to New Composite for Orthopaedic Use," *Int. J. Mater. Eng.*, vol. 2014, no. 3, pp. 103–113, 2014, doi: 10.5923/j.ijme.20140403.06.

[18] F. Sotehi, D. Benzerga, A. Haddi, A. Chouiter, and B. Abderrahmane, "Numerical analysis of cracking at the nozzle junction in a distillation column," *Res. Eng. Struct. Mater.*, pp. 1–19, 2025, doi: http://dx.doi.org/10.17515/resm2025-663me0207rs.

Appendix 01:

Table 5. Parametric analysis of repair performance: Effect of welding current and tungsten inclusion size on maximum stress and residual lifetime for TIG and hybrid (TIG+CFRP) repairs

	Initial, damaged & TIG repaired (20µm inc)					Max Normal Stress: Hybrid repair [MPa]	Residual lifetime (years)
#	applied current, [A]	Max Normal Stress [MPa]	Max Residual Stress [MPa]	Max Equivalent Stress [MPa]	Residual lifetime (years)		
Intact state (benchmark)	-	205.4	-	-	~20	-	-
Cracked structure	-	634.3	-	-	5.1	-	-
perfect TIG	120	463.61	273.64	517.5	8.44	-	-
0.02 mm (inclusion size)	200	740.48	646.64	669.71	4.68	425.98	11.02
	160	682.92	608.6	647.4	5.09	407.31	12.41
	120	662.96	570.56	625.12	5.87	388.63	14.04